

A HELIOSEISMIC SURVEY OF NEAR-SURFACE FLOWS AROUND ACTIVE REGIONS AND THEIR ASSOCIATION WITH FLARES

D. C. BRAUN

NorthWest Research Associates, 3380 Mitchell Lane, Boulder, CO 80301, USA

accepted Astrophys.J. Jan 28, 2016

ABSTRACT

We use helioseismic holography to study the association of shallow flows with solar flare activity in about 250 large sunspot groups observed between 2010 and 2014 with the Helioseismic and Magnetic Imager on the Solar Dynamics Observatory. Four basic flow parameters: horizontal speed, horizontal component of divergence, vertical component of vorticity, and a vertical kinetic helicity proxy, are mapped for each active region during its passage across the solar disk. Flow indices are derived representing the mean and standard deviation of these parameters over magnetic masks and compared with contemporary measures of flare X-ray flux. A correlation exists for several of the flow indices, especially those based on the speed and the standard deviation of all flow parameters. However, their correlation with X-ray flux is similar to that observed with the mean unsigned magnetic flux density over the same masks. The temporal variation of the flow indices are studied, and a superposed epoch analysis with respect to the occurrence to 70 M and X-class flares is made. While flows evolve with the passage of the active regions across the disk, no discernible precursors or other temporal changes specifically associated with flares are detected.

Subject headings: Sun: activity, Sun: flares, Sun: helioseismology, Sun: magnetic fields, sunspots

1. INTRODUCTION

A fundamental question in solar physics is how magnetic fields emerge from the solar convection zone into the solar atmosphere and then develop solar eruptions such as flares and CMEs (Fan 2009; Schrijver 2009). It is widely held that highly twisted magnetic fields, emerging perhaps into a pre-existing field, are required for the formation of active regions producing M- or X-class flares (Schrijver 2009). Observations of the linkage between subsurface flows and the twist, electric current content, and other properties of active regions (hereafter ARs) are important to understand, and perhaps even predict, the flare phenomenon. Considerable effort has been spent in studying the time evolution of magnetograms or continuum images of active regions in order to quantify photospheric motions which may lead to predictive indices (e.g. Leka & Barnes 2007; Schrijver 2007; Welsch et al. 2009). Helioseismic measurements of subsurface motions extend the spatial volume over which AR properties, and their role in transporting magnetic helicity and current into the corona, can be explored. In addition, the direct inference of mass flows complements measurements of photospheric motions of (magnetic or continuum) features (Wang et al. 2011; Beueregard et al. 2012; Wang et al. 2014).

Any detection and interpretation of photospheric or subsurface flow precursors to flares requires understanding the pre-existing flow fields, and their general characteristics, associated with active regions. Photospheric outflows (called “moats”) extending past the penumbrae of most sunspots have been studied for decades (Brickhouse & LaBonte 1988). Larger converging flows around active regions were first detected using local helioseismology (Gizon et al. 2001; Haber et al. 2001). Inverse modeling using ring-diagram (hereafter RD) analy-

sis performed by Haber et al. (2004) indicated these converging flows are situated above deeper outflows. A consensus appears to be that these flows have speeds on the order of 50 m s^{-1} which may extend out to as much as 30° from the AR centers. However, Braun & Wan (2011) found that most outflows around ARs are compact and have flow speeds typical of the surrounding supergranulation.

Komm et al. (2004) first began to systematically characterize AR flows, deduced from low-resolution RD analysis, in terms of their horizontal divergence and their vertical components of vorticity and kinetic helicity. That work was the first to detect a hemispheric preference for the vertical vorticity of the flows, which was cyclonic over the 15° spatially-averaged flows both with and without the removal of a large-scale differential rotation pattern. Using ring-diagram procedures with considerably higher resolution, Hindman et al. (2009) examined the divergence and vortical components of motions within about 200 magnetic regions. They confirmed cyclonic motions near active region boundaries, but also demonstrated an anticyclonic trend associated with the cores of the ARs which are presumably dominated by the sunspot moats. More recently, Komm & Gosain (2015) have compared the hemispheric preference, for long-lived activity complexes, of both the subsurface kinetic helicity, determined from ground-based observations from the Global Oscillation Network Group (GONG), and the current helicity as determined from synoptic vector magnetograms.

Specifically to examine the relation between subsurface flows, deduced from from (low-resolution) RD analysis, and solar flares, Mason et al. (2006) surveyed the subsurface vorticity of ARs over 43 Carrington rotations using GONG and over 20 rotations observed using data from the Michelson Doppler Imager (MDI) instrument on the SOHO spacecraft. Both data exhibited a trend between the unsigned vorticity and the product of the

logarithm of flare intensity and maximum unsigned magnetic flux, for ARs above a given flux threshold. An expanded version of the GONG RD-based survey was used by Komm & Hill (2009) to demonstrate a correlation between X-ray flux and vorticity, with both quantities averaged over the disk passage of the ARs. The flow measurements from this survey subsequently provided the basis for the development of an empirically-based parameter, based on the subsurface kinetic helicity density, which showed specific temporal variations 2-3 days before flares (including C, M, and X-class events; Reinard et al. 2010). Applying discriminant analysis to a variety of both magnetic and subsurface-flow parameters, Komm et al. (2011a) suggest that the subsurface flow parameters improve the ability to distinguish between flaring and non-flaring ARs.

Using a much smaller sample of 5 flaring ARs, but employing time-distance helioseismic methods with considerably higher spatial resolution, Gao et al. (2014) found sporadic and short-duration changes (called “bumps”) in the kinetic helicity which, slightly more than half the time, occurred within about 8 hours (before or after) an X-class flare.

The primary goal in this study is to examine the association with solar flares of near-surface flows within solar magnetic regions. This association may include: (1) the predilection of flares to occur in regions with specific flow properties, and (2) any precursor of, or response to, specific solar flares visible in the temporal evolution of the flow patterns. To do this we make use of nearly five years of nearly continuous and high resolution SDO/HMI observations of approximately 250 of the largest sunspot groups cataloged by NOAA. Our motivation is not to reproduce or confirm any prior study, but to exploit the high-resolution capabilities of helioseismic holography to perform an independent examination of the flows within the largest active regions. It is necessary to place any observed association (or lack thereof) between flows and flares in the proper context. Consequently, a sub-goal is to provide a survey of the general near-surface flow properties of large NOAA sunspot groups. For this study, we focus our attention on specific flow parameters which can be derived from inferences of the two-dimensional near-surface vector flow field, including the horizontal component of the divergence and the vertical component of the vorticity. We also examine the product of these, which provides a proxy for the vertical component of kinetic helicity (Rüdiger et al. 1999; Komm et al. 2007). A fourth parameter is the speed of the horizontal flow. Averages and standard-deviations of these basic parameters, assessed over spatial masks constructed using HMI magnetograms, provide a set of indices with which we search, using scatter plots and superposed epoch analysis, for correlations with solar flare activity.

2. ACTIVE REGION SELECTION

The sample of active regions we consider consists of all sunspot groups assigned a number by NOAA between the start of HMI observations (2010 May) and 2014 December, and which reached a size of at least 200 micro-hemispheres (hereafter μH). Although complete records of the the sunspot group properties are available¹, for

convenience we used the sunspot database maintained at NASA Marshall Space Flight Center² which provides daily averages of the sunspot group properties including size and Carrington coordinates.

We identified 252 regions which met these criteria, which represent approximately the largest 20% of all NOAA numbered sunspot groups. Our survey includes a single region (AR 12017) which had a maximum area of only 160 μH but was responsible for 23 flares including an X-class flare. Our final sample includes ARs responsible for all (43) X-class flares, 86% (≈ 460) of the M-class flares, and 72% (≈ 3600) C-class flares occurring during this time period.

In spite of the size criteria for selection, the sample includes cases of relatively quiescent ARs which provide a basis for comparison with the more flare productive ones. For example, 137 ARs in the sample (i.e. slightly more than half) produced neither M nor X-class flares and 17 of those produced no C-class flares either. Unfortunately for the statistician, the Sun does not appear to emerge large numbers of flare-free magnetic regions with a distribution of properties (e.g. size, sunspot number, magnetic flux) which otherwise match the flaring regions. There are likely diminishing (and even detrimental) returns in including smaller flare-free regions in our survey. That being said, we need to be mindful of selection bias when (1) assigning meaning (e.g. cause-and-effect) to associations of flows and flares, and (2) generalizing observations or inferences about the flow properties of our sample to other types of active regions.

For each AR, a 9.1 day long datacube is constructed from a Postel’s projection of the full-disk HMI Dopplergrams and centered on the Carrington coordinates averaged over its disk passage. The remapped datacube spans 30° by 30° with a pixel spacing of 0.0573° . and is divided into 16 non-overlapping intervals of 13.6 hr duration for helioseismic analysis. For context, a set of remapped, cospatial and time-averaged line-of-sight HMI magnetograms for each interval is constructed, using full-disk magnetograms sampled every 68 minutes. Time intervals for which the mean AR location was greater than 60° from disk center, or for which gaps in the HMI data exceeded 30% of the 13.6 hr period are excluded from the survey. We are left with 3908 sets of helioseismic measurements, defining a set to be a single AR observed over a unique 13.6 hr interval.

3. HELIOSEISMIC HOLOGRAPHY

Helioseismic holography (hereafter HH) is a method which computationally extrapolates the surface acoustic field from a selected area or “pupil” into the solar interior (Lindsey & Braun 1997) in order to estimate the amplitudes of the waves propagating into or out of a focus point at a chosen depth and position in the solar interior. These amplitudes are called the acoustic ingression and egression respectively. To study travel-time anomalies sensitive to the flows one constructs cross covariances between the ingression and egression amplitudes using pupils which take the form of an annulus divided into quadrants. This type of pupil configuration is the basis for “lateral vantage” HH (Lindsey & Braun 2004), to which deep-focus methods in time-distance helioseis-

¹ <http://ngdc.noaa.gov/stp/space-weather/solar-data/solar-features/sunspot-locations/> ² <http://psb12a01.cas.nasa.gov/greenwch.shtml>

mology and common-depth-point reflection seismology methods are analogous. For the results presented here, we choose a focus depth 3 Mm below the surface.

Travel-time measurements sensitive to horizontal flows are extracted from cross-covariances between the egressions and ingressions computed in pupils spanning opposite quadrants which extend in the east, west, north and south directions from the focus. The methodology is described in detail in prior publications (e.g. Braun et al. 2007; Braun & Birch 2008; Braun 2014). The steps include: (1) compute the 3D Fourier transform of the Postel-projected data in both spatial dimensions and in time, (2) extract the data within the frequency bandpass 2.5 – 5.5 mHz, (3) apply a phase-speed filter, (4) compute egression and ingression amplitudes with the appropriate Green’s functions, (4) compute egression–ingression correlations, and (5) measure travel-time differences. The filter employed in step (3) helps to reduce noise with high spatial-frequency. It consists of a Gaussian function of phase speed with a full width at half maximum of 9.2 km s⁻¹ and is centered at 18.8 km s⁻¹ which is tuned to waves propagating horizontally at a depth of 3 Mm. The design and utility of filters for lateral vantage HH is discussed further by Braun (2014). Step (4) is computed by convolutions of the data cube with Green’s functions computed with the eikonal approximation and using a plane-parallel approximation, which is well suited for the shallow focus depth of 3 Mm. Braun (2014) explores the validity of this approximation in detail. The products of these analyses are maps of travel-time shifts $\delta\tau_{ns}$, and $\delta\tau_{we}$, which represent standard north-south and west-east travel-time differences.

3.1. Flow calibration

Rather than carry out inverse modeling of the travel-time shifts to infer the three-dimensional variation of the flows, we employ a simple calibration procedure. This minimizes complications and uncertainties, due to the presence of strong photospheric magnetic fields, in the inversion methods (e.g. DeGrave et al. 2014). Travel-time shifts are related to the actual flows through a convolution of the true flow components and the appropriate sensitivity functions. For our measurements with a focus depth of 3 Mm, the sensitivity functions are sufficiently compact in volume so as to render the travel-time differences reasonable proxies for the horizontal components of the near-surface flows themselves. HH analyses of near-surface flows using travel-time shifts as flow proxies have been carried out in prior studies (e.g. Braun et al. 2004; Braun & Wan 2011; Birch et al. 2013). Here, the travel-time differences τ_{we} and τ_{ns} are calibrated into westward and northward vector components of a horizontal depth-independent flow (u_x, u_y) by applying two different tracking rates to the same region of the Sun. These rates consist of (1) the nominal Carrington rotation rate and (2) the nominal Carrington rate plus a constant offset. The tracking offset divided by the shift in τ_{we} between the sets of measurements yields a calibration factor of -7.5 relating the speed (in units of m s⁻¹) to the travel-time difference (in s). The minus sign reflects the fact that a positive flow directed to the north (west) produces a reduction in the corresponding north-south (west-east) time difference. The range over the depth to which our calibrated flow is sensitive is discussed in Braun et al.

(2007), which shows the sensitivity function computed under the Born approximation, for lateral-vantage HH at a 3 Mm focus-depth. The function has a broad contribution which is peaked around 3 Mm depth. Approximately 60% of the sensitivity occurs between depths of 2–5 Mm, with a 30% (10%) sensitivity for shallower (deeper) flows.

4. FLOW PARAMETERS

Motivated by the the results of prior helioseismic surveys or analyses of specific active-region flows, we consider several flow parameters for study. These include the vertical component of the vorticity

$$\text{VOR} = \frac{\partial u_y}{\partial x} - \frac{\partial u_x}{\partial y},$$

and the horizontal divergence

$$\text{DIV} = \frac{\partial u_y}{\partial x} + \frac{\partial u_x}{\partial y}.$$

We also include a proxy for the vertical contribution to the kinetic helicity (Rüdiger et al. 1999; Komm et al. 2007)

$$\text{HEL} = \text{VOR} \cdot \text{DIV},$$

and the horizontal speed

$$|V| = \sqrt{u_x^2 + u_y^2}.$$

The proxy HEL is related to the vertical component of the true kinetic helicity by a substitution of the horizontal divergence for the vertical component of the flow, with the ratio of the two given by the density scale height in the anelastic approximation (Rüdiger et al. 1999).

If x and y denote westward and northward directions respectively, then the sign of VOR as defined above is positive (negative) for counterclockwise (clockwise) vortical motion as viewed from above the solar photosphere. Prior analyses have shown that the vertical vorticity and kinetic helicity, with this sign convention, have antisymmetric properties, at least statistically, with respect to the equator. This is true for convective motions in both the quiet-Sun (supergranulation) field (Duvall & Gizon 2000) and for motions within active regions (Komm et al. 2007). To facilitate the combination of flow quantities measured in ARs from both hemispheres, we switch the sign of VOR in the southern hemisphere, so that over the entire Sun a positive (negative) value of VOR is indicative of cyclonic (anticyclonic) motions. A positive VOR, for example, implies counterclockwise rotation in the northern hemisphere and clockwise rotation in the southern hemisphere.

4.1. Example: AR 11263

Figure 1 shows maps of the four basic flow parameters, compared to time-averaged line-of-sight magnetograms, for three consecutive time intervals and centered on AR 11263. The derivatives for evaluating VOR and DIV are computed in the Fourier (horizontal wavevector) domain. To minimize high-frequency noise all of the maps are smeared with a two-dimensional Gaussian with a FWHM of 0.48° (5.8Mm). This region reached a maximum size of 720 μ H (larger than 90% of the sample) and was responsible for one X-class flare and 3 M-class flares. Qualitatively the features visible in the flow-parameter maps

of AR 11263 are fairly typical for our sample. The largest speeds, reaching nearly 1 km s^{-1} , are found surrounding sunspots and are associated with the moat flows. These moats also produce the largest diverging signals in the DIV maps. Surrounding these outflows in the DIV maps are regions of converging flows which extend, at most, a few degrees beyond the moats. The vorticity and helicity maps exhibit complex patterns composed of compact features with both signs and sizes as small as the resolution imposed by our 0.48° smearing. There is a clear enhancement of the vorticity (and helicity) signals within the strongest magnetic regions. Although some fraction of these signals may be attributed to the effects of realization noise, a careful examination of the maps reveals features which persist from one 14 hr interval to the next. Successive vorticity maps, masked to isolate only regions with flux densities greater than 500 G, are correlated with values of Pearson’s coefficient equal to about 0.4. Successive divergence maps have typical Pearson’s coefficients of about 0.6.

Supergranulation in the magnetic-free regions have peak speeds on the order of $\approx 300 \text{ m s}^{-1}$ which appear as ring-like features (weaker than the sunspot moats) in the maps of $|V|$ and diverging centers surrounding by converging lanes in the DIV maps.

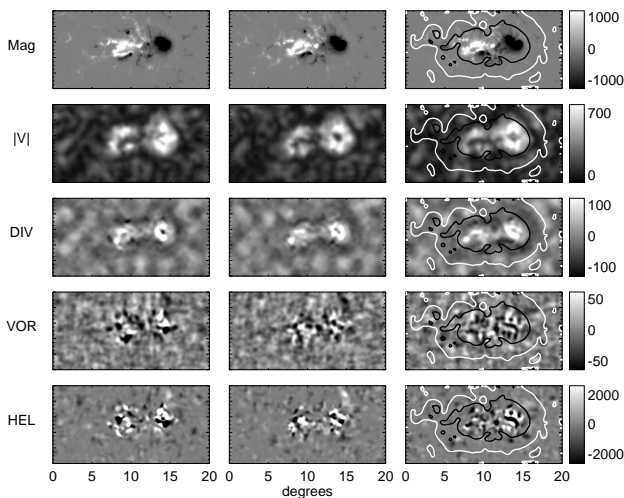


Figure 1. Magnetograms and flow parameter maps for AR 11263 for three successive time intervals. From the top row down are maps of the: line-of-sight HMI magnetograms, near-surface horizontal speed $|V|$, divergence (DIV) proxy, vorticity (VOR) proxy and kinetic helicity (HEL) proxy (as defined in the text). The three columns indicate successive 13.6 hr non-overlapping intervals over which the quantities shown are obtained. The middle column represents observations centered at 2011 Sept 4 00:58 UT. The contours in the right-most column define magnetic-field flux densities of 50 (white) and 200 G (black) derived using a potential-field extrapolation and smoothed for the purpose of this figure. The grayscales cover the range of values indicated, with scales in units of G for the magnetograms, m s^{-1} for the speed $|V|$, 10^{-6} s^{-1} for DIV and VOR, and 10^{-12} s^{-2} for the helicity proxy HEL.

Our aim is to quantitatively condense the spatially complex maps, shown for example in Figure 1, into manageable “flow indices,” which represent the the first and second moments of their distribution over regions isolated by masks. It is the magnetic field which must, by most conceivable means, link any near-surface flow

with the flaring process. Consequently, the purpose of the mask is to isolate the flows in magnetically relevant pixels for further analysis. Recognizing that what defines “relevant” is unknown, we select different thresholds of photospheric magnetic field to construct these masks. Specifically, two sets of masks with minimum flux-density thresholds set at 50 and 200 G are used. The masks provide alternately a fairly generous or restrictive definition of a magnetic region, with the goal to establish whether and how the results we obtain depend on this choice. We note that the stronger threshold primarily isolates the sunspots and their immediate vicinities while the weaker value includes considerable surrounding field. Figure 2 shows pixel histograms for our flow-parameter maps for one interval centered on AR 11263 using the different masks.

A strict use of the (unsigned) line-of-sight magnetograms can produce highly discontinuous masks due to, for example, false neutral lines in sunspot penumbrae which appear when the spots are near the limb. Consequently, we use thresholds based on maps of a potential-field extrapolation of the total field, B_p , from the line-of-sight magnetograms. All of the masks are limited in the spatial domain by a “bounding box” spanning 20° in longitude and 10° in latitude and centered on each NOAA AR coordinate (e.g. the area shown in Figure 1). This box was adequate for most of the active regions in our sample, however five regions (ARs 11339, 11520, 11944, 11967, and 12192) extend well beyond this area. Consequently a larger ($20^\circ \times 20^\circ$) bounding box was used for these five regions. For the purpose of comparison, we also construct a “quiet mask” which consists of all pixels within the bounding box with $|B_p| < 50\text{G}$. Distributions for the flow parameters using these masks are indicated by different colored histograms in Figure 2. Hereafter, we refer to the three masks as the “200+ G mask,” “50+ G mask,” and “quiet mask” respectively.

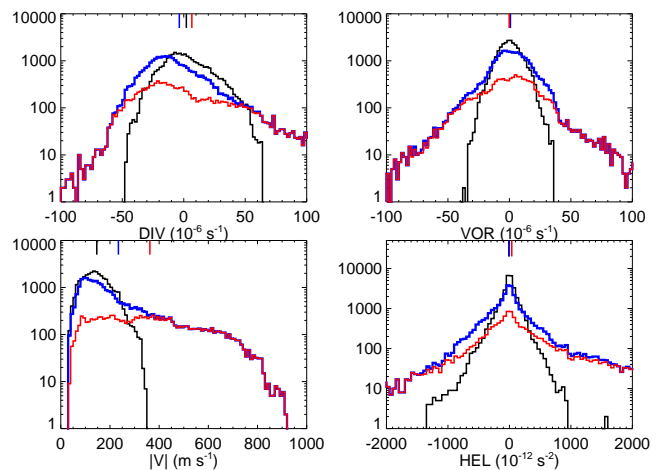


Figure 2. Distributions of the four flow parameters, DIV, $|V|$, and HEL for one interval centered on AR 11263. The colors indicate histograms of each flow parameter over different masks defined by the (potential-field) magnetic flux-density B_p : $|B_p| > 200\text{G}$ (red), $|B_p| > 50\text{G}$ (blue) and $|B_p| < 50\text{G}$ (black). The mean values of each distribution are indicated by the vertical markers, with appropriate color, descending from the top of each panel. Note that in the wings of the distributions, the red and blue curves are nearly the same.

The distributions in Figure 2 are substantially wider for magnetic pixels than for the quiet mask, confirming the impression obtained by a visual examination of the maps (e.g. Figure 1). It is also evident that the largest values of all the flow parameters are confined within the 200+ G mask, which causes the wings of the histograms for the 200+ and 50+ G cases to coincide nearly identically. While VOR and HEL distributions are nearly symmetric about zero, the distributions of the divergence parameter DIV are skewed for all masks, even for the quiet pixels. Prior studies of supergranular flows have also demonstrated asymmetric distributions of the horizontal divergence (e.g. Duvall & Gizon 2000). It is also evident that, for the example interval shown in Figure 2, the DIV parameter has a mean value which is positive (diverging flows) for the 200+ G mask, and negative (converging flows) for the mask constructed with the lower 50 G threshold. The former value is consistent with Figure 1 where it can be seen that the 200+ G mask fully contains the diverging sunspot moat. The 50+ G mask includes both the sunspot moats and apparently a sufficient area of converging flow surround the moats to outweigh their contribution in the spatial average.

In studies of flows averaged over substantially larger areas, such as with low-resolution RD methods, large-scale motions such as differential rotation are often removed from the data in order to isolate weaker AR-related flows (e.g. Komm et al. 2004, 2007). This is neither necessary nor desired with the strong compact flow signals revealed with high-resolution HH. For reference, at a typical AR latitude of 15° , the differential rotation contributes a background vorticity of about $0.3 \times 10^{-6} \text{ s}^{-1}$. This is two orders of magnitude below the largest signals observed within the AR masks as shown in Figures 1 and 2, and at any rate varies little across the dimensions of the magnetic masks.

4.2. Sample Distributions

We consider for further analysis the set of 16 flow indices which consist of the mean and standard deviations of the four basic flow parameters within either of the two flux-density masks. We use a notation such that, e.g. for the DIV parameter, the quantities $\langle \text{DIV} \rangle_{50+}$ and $\text{std}(\text{DIV})_{50+}$ represent the mean and standard deviation of DIV over the pixels in the 50+ G mask, and $\langle \text{DIV} \rangle_{200+}$ and $\text{std}(\text{DIV})_{200+}$ represent the analogous indices over the 200+ G mask. This is also applied for the other 12 indices computed from the three parameters VOR, HEL, and $|V|$ and the two masks. An additional 8 indices, representing the mean and standard deviations of the four flow basic parameters, over the quiet pixels within the bounding box, are also computed for purposes of comparison. These indices are denoted with a subscript q : for example, $\langle \text{DIV} \rangle_q$ and $\text{std}(\text{DIV})_q$.

The indices $\langle \text{DIV} \rangle$, $\langle \text{VOR} \rangle$, and $\langle \text{HEL} \rangle$ are signed quantities, while $\langle |V| \rangle$, $\text{std}(\text{DIV})$, $\text{std}(\text{VOR})$, $\text{std}(\text{HEL})$, and $\text{std}(|V|)$ are not. We find a systematic variation in the unsigned quantities with distance of the AR from the center of the disk. For example, Figure 3 illustrates this systematic variation for the index $\langle |V| \rangle_{200+}$. Errors due to foreshortening may introduce noise for the helioseismic measurements performed away from the center of the disk. This noise appears to be enhanced in ARs and is possibly related to the suppression of wave am-

plitudes in magnetic areas. The result is that the signed indices show spurious temporal variations as the AR rotates across the disk, with higher (lower) values near the limbs (disk center). To remove this variation from each of the signed flow indices, a correction factor $f(\mu)/f(1)$ is divided out of the uncorrected measurements, where f is a quadratic fit to the data (e.g. Figure 3). No corrections are applied to the signed indices for which trends with distance from the central meridian (from east limb to west limb), or with heliocentric angle, appear to be negligible (i.e. produce trend-related deviations on the order of a few percent or less of their standard deviation). Artifacts, which appear as pseudo flows pointing towards or away from disk center, are well known in other helioseismic measurements (e.g. Duvall & Hanasoge 2009; Zhao et al. 2012; Baldner & Schou 2012). We note that these large-scale low-amplitude ($\leq 10 \text{ m s}^{-1}$) artifacts are very small compared to the flows observed within our spatially compact (AR-sized) masks.

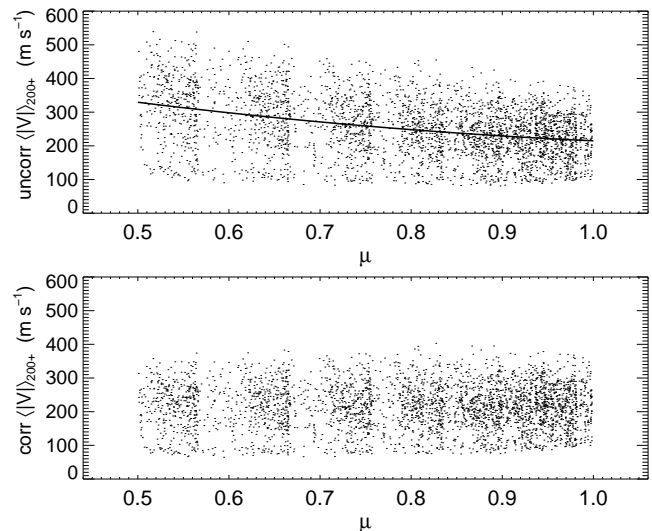


Figure 3. Top panel: uncorrected values of the speed $|V|$, averaged over magnetic pixels with $|B_p| > 200\text{G}$, as a function of μ , the cosine of the heliocentric angle. The solid line indicates a quadratic polynomial fit f to the data. Bottom panel: corrected values of $|V|$ after dividing out the normalized function $f(\mu)/f(1)$.

Figure 4 presents histograms of eight of the flow indices for the entire sample of measurements. We also include for comparison the distributions of the same four parameters determined using the quiet-pixel masks. Not shown (for brevity) are the distributions of the indices based on the standard deviations of the four basic parameters. Qualitatively, they resemble the distributions of the unsigned indices based on averages of $\langle |V| \rangle$, which are shown in the lower-left panel of Figure 4. In Figure 4, about 280 (or 7% of the total) sets of measurements are excluded from the histograms for which the number of pixels in the 50+ G mask fell below 10^4 , which is about one-third of the median area over the sample. This cut-off effectively removes measurements centered on an active region during time intervals prior to its eventual emergence in the photosphere.

There are a number of items worth noting in this figure. The broadest distributions are observed for indices derived with the 200+ G mask. Thus, the strongest vari-

ation in the flow indices, among different ARs and time intervals, occurs in the strongest magnetic regions. In addition, the spatially averaged DIV indices have clear sign preferences, depending on the magnetic mask. Averaged over the 50+ G mask, the divergence is overwhelmingly negative, while the opposite is true for the 200+ G mask. The nearby quiet regions have a distribution in $\langle \text{DIV} \rangle$ which is largely positive. It is plausible that this arises in large measure from the presence of flows directed into the ARs which originate in the nearby quiet pixels and cross over the boundary defined by the 50 G threshold. The averaged vorticity index for the 50+ G mask also shows a clear (cyclonic) sign preference, but the quiet pixels and those above the 200 G threshold show a more symmetric distribution about zero. Nevertheless, there is a clear preference for negative helicity as averaged over all (even quiet) masks. This arises if the spatially averaged values of DIV and VOR are anti-correlated, as one might expect from the action of the Coriolis force due to solar rotation.

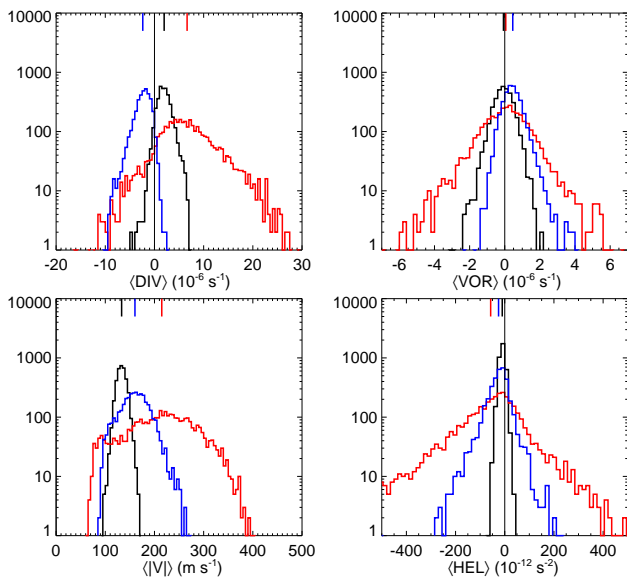


Figure 4. The distributions over the sample of measurements of several of the spatially-averaged flow parameters. The red, blue, and black histograms represent spatial averages over the 200+ G, 50+ G, and quiet masks respectively (see text). The mean of each distribution is shown by the vertical marker, with the appropriate color, descending from the top of each panel.

4.3. Flare Productivity

Before exploring the time variation of the flow indices, we examine the overall correlation between the indices with flare productivity over all ARs and time intervals. We use NOAA event reports³ which record the integrated X-ray flux (in J m^{-2}), times of the peak X-ray flux, and associated active region number, for solar flares as observed with the GOES spacecraft. For each AR and each 13.6 hr time interval, we integrate the X-ray flux of any observed flares in that AR and time to produce a measure of the flare productivity. We first examine scatter

plots of each of our flow indices against the this flare productivity. For brevity, Figures 5 and 6 condenses the correlations indicated by these scatter plots into binned averages of the 24 indices (i.e. the 16 AR indices and 8 quiet indices) as functions of the X-ray flux. In general, the signed indices for the 50+ and 200+ G masks and their quiet-mask counterparts exhibit little variation with flare productivity. However, the the mean divergence assessed over the 200+ mask shows an apparent decrease with increasing X-ray flux. Further examination reveals a similar (decreasing towards zero) trend of the mean divergence with other indicators of the size of the active region, such as the integrated magnetic flux, or simply the number of pixels, in the 200+ G mask. The exact reason for this is unknown, but seems to indicate an increasing contribution of converging flows to the 200+ G mask as the size of active regions increases, even while the mean divergence over the larger 50+ G mask stays nearly constant.

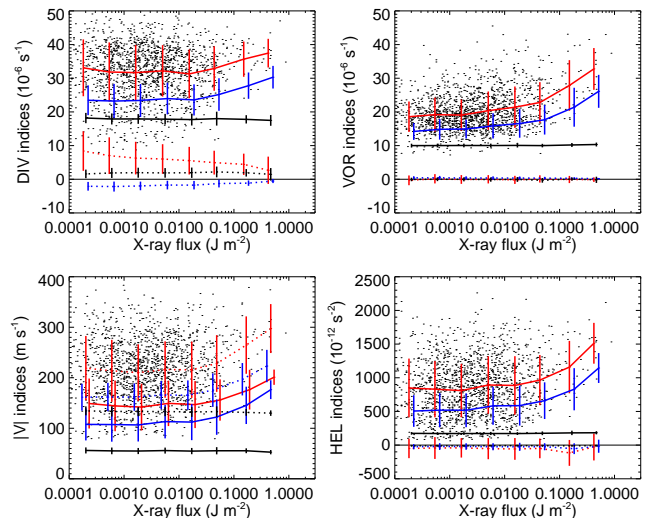


Figure 5. Flow indices as functions of the flare productivity, defined as the integrated X-ray flux summed over all flares within each AR and 13.6 hr time interval included in our survey. The dotted (solid) lines connect flux-binned averages of indices representing the mean (standard deviation) of the flow parameters indicated on the vertical axes. The colors indicate the mask used, where red, blue and black curves indicate the 200+ G, 50+ G, and quiet masks. The vertical bars indicate the range defined by the average \pm one standard deviation for all points within bins of the (logarithm of the) X-ray flux. For clarity, the scattered points show only the individual measurements which went into the averages indicated by the top-most curve in each panel. The vorticity and helicity indices based on the mask averages (dotted curves) are difficult to discern in the two right panels and are replotted in Figure 6 with an expanded vertical scale.

The unsigned indices $\langle |V| \rangle$, $\text{std}(\text{DIV})$, $\text{std}(\text{VOR})$, $\text{std}(\text{HEL})$, and $\text{std}(|V|)$ over both magnetic masks show increases for the most flare-active intervals (i.e. when the X-ray flux exceeds about 0.1 J m^{-2}). The amount of this increase is modest when compared to the spread of the measurements. Moreover, the correlation is similar to that observed with other magnetic properties. Figure 7 shows that the averaged unsigned magnetic flux density, over either the 50+ or 200+ G masks, has a similar dependence with X-ray flux. The similarity of the correlations between Figures 5 and 7 raises the question

³ <http://ngdc.noaa.gov/stp/space-weather/solar-data/solar-features/solar-flares/x-ray/>

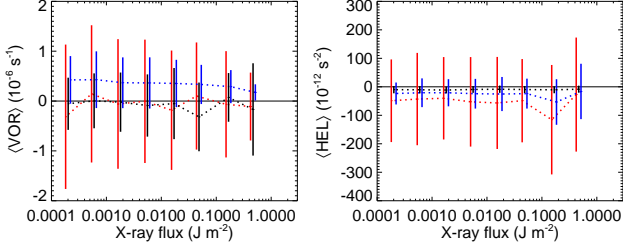


Figure 6. The indices based on the spatial averages of the vorticity (left panel) and helicity (right panel) as functions of the X-ray flux. These are the same quantities as shown in the right panels of Figure 5 but with expanded vertical scales. The red, blue, and black curves indicate the results for the 200+ G mask, 50+ G mask, and the quiet pixels, respectively. The vertical bars indicate the range defined by the average \pm one standard deviation for all points within bins of the (logarithm of the) X-ray flux.

of whether there exists a physical link between the observed flow parameters and the onset of flares, or rather simply that larger ARs provide a preferred environment for both increased flows and (as is already known) flare occurrence.

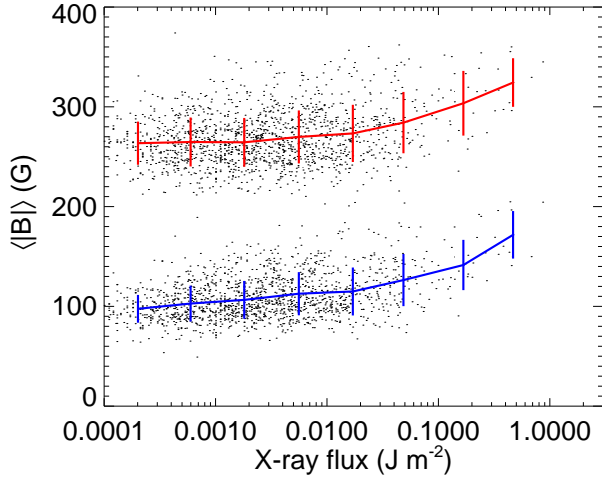


Figure 7. Scatter plots, with binned averages, of the unsigned magnetic flux density averaged over the 200+ G (red) and 50+ G (blue) masks respectively, as functions of the integrated flare X-ray flux.

5. TIME VARIATION OF FLOW PARAMETERS

Figures 8 and 9 show examples of the temporal variations of the flow indices for two ARs. One of these regions, AR 11283 was the site of one X-class flare and 3 M-class flares, while the other, AR 11363 was a large, but relatively flare-free region (producing only 8 C-class flares during its passage). The indices are plotted in terms of their fractional deviation from a temporal mean. For the unsigned indices, e.g. $\text{std}(\text{VOR})_{50+}$, this takes a form

$$\Delta \text{std}(\text{VOR})_{50+} \equiv \frac{\text{std}(\text{VOR})_{50+} - \overline{\text{std}(\text{VOR})_{50+}}}{\overline{\text{std}(\text{VOR})_{50+}}},$$

where the horizontal bar denotes the average over time. For the signed quantities, the change is relative to the

corresponding time-average of the standard-deviation based index, e.g.

$$\Delta \langle \text{VOR} \rangle_{50+} \equiv \frac{\langle \text{VOR} \rangle_{50+} - \overline{\langle \text{VOR} \rangle_{50+}}}{\overline{\text{std}(\text{VOR})_{50+}}},$$

and likewise for the other signed indices. For AR 11283, vertical lines denote the times of the X-class and M-class flares. It is inevitable that flows, and thus the flow indices, will change as an AR evolves. The two regions shown in Figures 8 and 9 highlight the dilemma in identifying flare-related flow changes. AR 11363 has no large flares, but both regions undergo evolution of at least some of the flow indices, e.g. $\Delta \text{std}(\text{HEL})_{50+}$ or $\Delta \text{std}(|V|)_{50+}$. In light of this, it is not clear how to interpret the variation of, say, $\Delta \text{std}(|V|)_{50+}$ immediately prior to the onset of the X-class flare in AR 11283 on 2011 Sept 6.

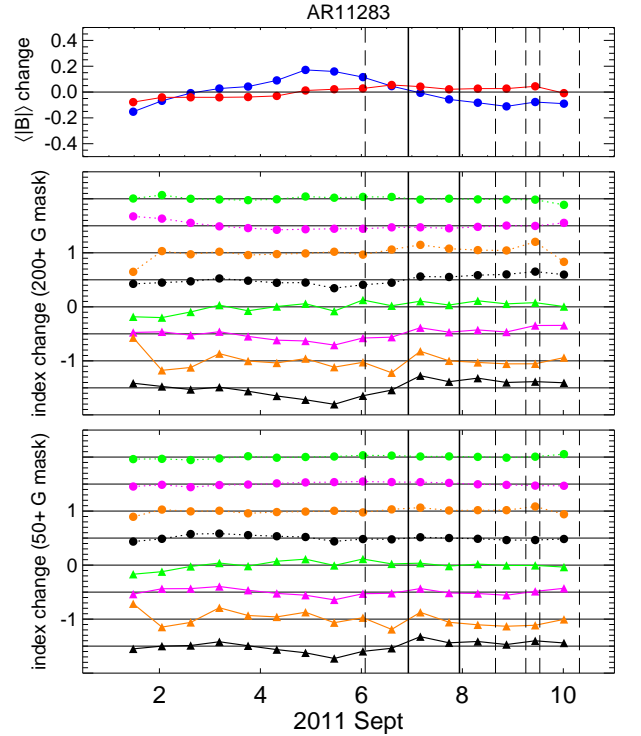


Figure 8. The variation in time of the mean unsigned magnetic flux density (top panel) and flow indices determined for the 200+ G mask (middle panel) and 50+ mask (bottom panel) G for AR 11283. All quantities are expressed in terms of their fractional change from the time-averaged quantity (see text for details). In the top panel, the red (blue) circles connected by lines of the same color, indicate the fractional change of the unsigned flux density averaged over the 200+ G (50+ G) masks. In the middle and bottom panels, the quantities shown are (from top to bottom) the fractional changes of: $\langle \text{VOR} \rangle$ (green circles), $\langle \text{DIV} \rangle$ (purple circles), $\langle \text{HEL} \rangle$ (orange circles), $\langle |V| \rangle$ (black circles), $\text{std}(\text{VOR})$ (green triangles), $\text{std}(\text{DIV})$ (purple triangles), $\text{std}(\text{HEL})$ (orange triangles), and $\text{std}(|V|)$ (black triangles). For clarity, each plot in the lower two panels is vertically displaced from the origin by multiples of 0.5 and denoted by the horizontal black lines. Solid (dashed) vertical lines denote the times of X-class (M-class) flares associated with this region.

Superposed Epoch (SPE) analysis (e.g. Mason & Hoeksema 2010; Reinard et al. 2010) of the flow indices provides one method to reduce the

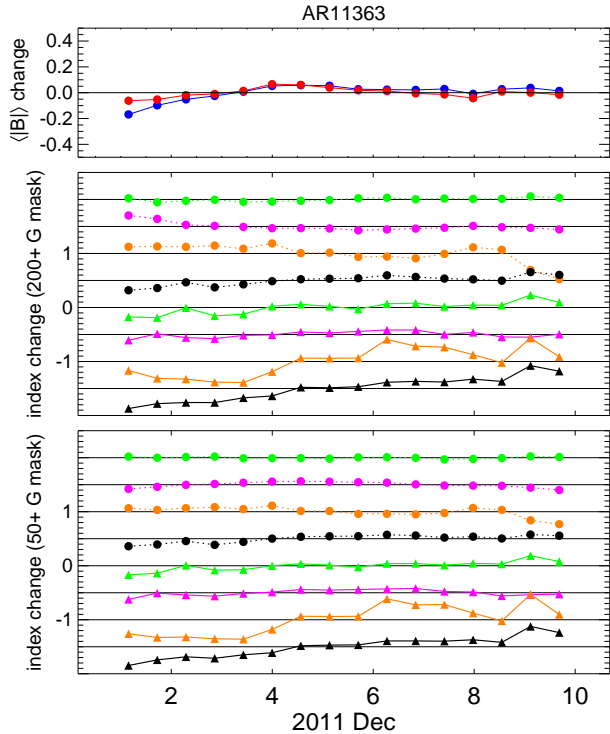


Figure 9. The variation in time of the unsigned magnetic flux density flow indices for AR 11363, shown in the same format as Figure 8. There are no X-class or M-class flares associated with this region during the dates observed.

influence of quiescent (non-flare related) evolution while revealing possibly subtle flare-related changes. To achieve this, we identify flare times from the NOAA GOES records of all X and M-class flares associated with the ARs in our survey. Each set of flow measurements are assigned to a 13.7 hr-long time bin, based on the midpoint in time of the HMI Dopplergrams used in the analysis relative to the time of the peak X-ray flux of the flare. The indices within each bin are averaged, using 6 bins before and 6 bins after the onset of flares. Thus, the analysis covers about 169 hr (6.8 days) of time around the occurrence of the flares. A data-coverage requirement was strictly enforced that, for any candidate flare, the relevant flow measurements are included in the SPE averages if, and only if, there are no gaps in those measurements over the entire 6.8 days. As discussed earlier, this may arise because of either unfavorable AR position (greater than 60° from disk center) or gaps in the HMI data. This requirement ensures an equal weighting, over the entire 6.8 days considered, of the contribution of each set of measurements. In spite of this restriction, we are left with 70 flares (associated with 34 distinct ARs) in our binned averages. We note that all X and M flares within each AR are included in the SPE analysis as the HH measurements allow, without rejection due to their proximity in time to other flares in the same region.

Figure 10 shows the results for the 70-flare average. Along with the flow indices, the figure also shows the SPE averages of the magnetic flux densities, determined over both the 50+ G and 200+ G masks. The averaged flux density show significant 5-10% quadratic-like varia-

tions with time relative to the flares. It is most likely that this results from foreshortening and projection effects related to the tendency of the AR to be positioned closer to the east (west) limb at early (later) times in the SPE averages than near the times of the flares. Indeed, without the center-to-limb detrending performed on the unsigned flow variables (e.g. Figure 3) one sees similar temporal variations of those quantities as well.

It is apparent (particularly by noting the units of the vertical scales), that the variations over time of the SPE averaged indices are considerably smaller than observed within individual ARs. For example, fractional variations of up to 40% in $\text{std}(\text{HEL})_{50+}$ or $\text{std}(|V|)_{50+}$ are present in Figures 8 and 9. The same quantities in the SPE-based averages show variations less than 10%. Moreover, although the latter variations are still notable, they are not substantially larger than expected from the standard error of the mean as indicated by the error bars. Most SPE-averaged flow indices, including the signed indices, exhibit time variations on the order of only a few percent over the entire 6.8 days. On the other hand, some variations do appear significant when, for example, compared to their standard errors. This includes variations in $\langle \text{DIV} \rangle_{50+}$, which show $\approx 3\%$ temporal variations which are on the order of three times the standard errors.

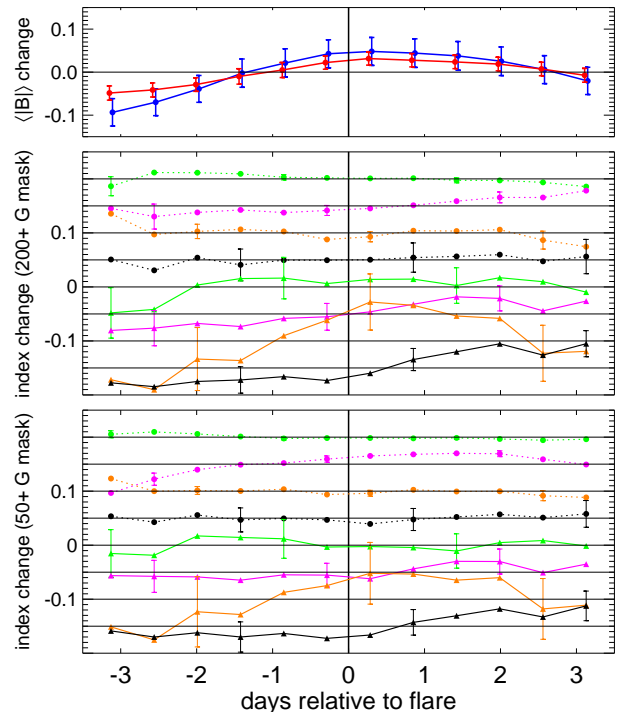


Figure 10. The variation in time of the SPE averaged flow indices over 70 X-class and M-class flares. The format is the same as for Figure 9 except that the abscissa shows the time offset in days from the midpoint of the bin intervals to the flare occurrence. Note that the vertical scale in all panels is substantially magnified compared to Figures 8 and 9 and that, in the lower two panels, offsets by multiples of 0.05 are applied to vertically separate each plot for clarity. Error bars represent the standard error of the mean. To avoid clutter, only representative error bars are shown.

To assess whether the observed variations in the SPE-averaged indices are associated with the specific occur-

rence of flares, we perform a separate SPE averaging procedure substituting the GOES flare list with an equivalent list with randomized times. In this control list each true flare-time is offset by either δ or $(\delta - 13)$ days, where δ is a random time between 0 and 13 days, and the choice is limited to the offset which keeps the AR visible to HMI. Pre-emergence intervals are excluded from the SPE by requiring a minimum pixel count of 10^4 over the 50+ G mask during the interval of the (pseudo) flare.

From this control list, we obtained the results shown in Figure 11, based on averages with respect to 71 pseudo flares. Compared with Figure 10, the similarity is quite striking. Just as in the SPE analysis with respect to actual X and M-class flare times, there are small, but significant temporal variations in several flow parameters. This is also apparently true for the magnetic flux density as well. Indeed, the similarity in the time variation of $\langle |B| \rangle$ for the two cases reinforces the likelihood of center-to-limb systematics, on the order of 5-10%, associated with the determination of the line-of-sight magnetic field. Many of the the flow indices, such as $\langle \text{DIV} \rangle$ and $\text{std}(\text{HEL})$, show significant variations with respect to the random times, for one or both magnetic masks, which are similar in magnitude to those observed with respect to the true flare times.

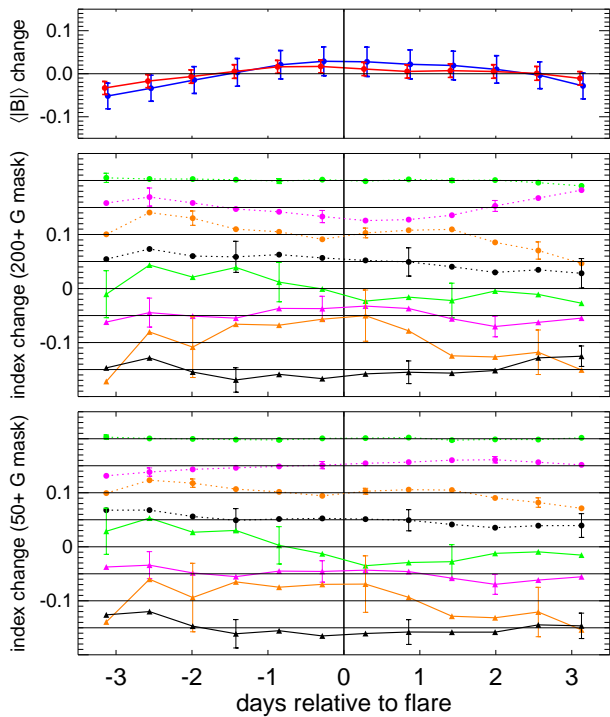


Figure 11. The variation in time of the SPE averages of flow indices with respect to a set of 71 random moments in time, selected by applying random offsets from the times of actual M and X-class flares.

We have performed SPE analysis over different flare classes (e.g. X-class flares alone, or flares defined by their integrated, rather than peak, X-ray flux). Decreasing the length of the time interval about flare occurrence increases the number of available measurements and therefore the statistics. However, in all cases examined, the

results are qualitatively the same as illustrated with the examples shown in Figures 10. We have also specifically examined the possibility of changes in the flow properties at time-scales shorter than 13.6 hr. For a subset of ARs, specifically those responsible for X-class flares, the HH analysis described in § 3 is repeated using datacubes 4.5 hr in length (one third the length of the original analysis). For this subsample of ARs, we find no compelling evidence for significant changes in the flow parameters on these shorter timescales.

6. DISCUSSION

We have carried out helioseismic survey of the near-surface flow parameters of 252 of the largest NOAA-numbered sunspot regions, spanning a 4.5 year interval between 2010 June and 2014 December. Although other comprehensive helioseismic surveys have been made, for example, with data from GONG, our survey includes flow measurements made with greater spatial resolution. The general properties of the horizontal flow divergence and vertical vorticity are similar to, and confirm, prior results made at lower resolutions (e.g. Komm et al. 2004; Hindman et al. 2009). Specifically, we see that the typical active region is characterized by strong outflows by sunspots in the AR centers, and surrounded by somewhat weaker converging counter cells. The vorticity signals are considerably weaker than those associated with the horizontal divergence, and likely include a larger fraction of realization noise. Nevertheless, active regions show small-scale vorticity signals significantly higher than surrounding quiet regions. The spatially-averaged kinetic helicity proxy for different magnetic masks indicate small rotational motion consistent with Coriolis forces acting on the converging or diverging flows components.

There is a modest correlation with integrated flare X-ray flux of several of the flow indices we examined, including the average speed, and the standard deviations over the magnetic masks of all four basic parameters (speed, divergence, vorticity and kinetic helicity). However these correlations strongly resemble those obtained with basic magnetic properties, such as the mean unsigned flux density. The similarity of the results between the choice of the flux-density threshold in the spatial masks shows that these correlations primarily arise for flows within or near the strongest flux and are little changed when weaker flux regions are included. Overall, the trends resemble at least qualitatively the findings of Komm & Hill (2009), albeit with substantially different flow parameters. We cannot at this stage rule out the possibility that information characterizing the near-surface flows may, along with magnetic indicators, help distinguish between flaring and non-flaring AR or even predict flares such as suggested by Komm et al. (2011a).

Some differences between our flow indices and those employed previously are worth noting. The “vorticity” indicators defined by Komm & Hill (2009) were constructed from relatively large spatial variations of the horizontal components of vorticity, unlike the vertical component examined in the present study. Furthermore, it is difficult to directly compare our near-surface indices with the parameter defined by Reinard et al. (2010) which is proportional to, among other factors, the spread in depth of kinetic helicity. On the other hand, in light of these results, it is reasonable to question why higher

resolution observations of converging flows (e.g. such as characterized by the divergence-based indices examined here) do not show stronger association with flaring regions than other indicators. This might be expected since converging flows presumably comprise the near-surface components of the “vortex rings” (Komm et al. 2011b) inferred from the ring-diagram results to be strongly associated with flaring regions.

We do not see, in our own flare indices, specific events occurring near flares and which resemble the bumps in the vertical component of kinetic helicity suggested by Gao et al. (2014). That study used direct inferences (from inverse modeling of time-distance travel-time shifts) of vertical velocities within 1 Mm of the photosphere, but their kinetic helicity parameter is otherwise directly comparable to our own proxy HEL. We note that Gao et al. (2014) used shorter, overlapping, time intervals (i.e. 8-hr long analyses spaced every 4 hr) but looked at a much smaller sample of flaring regions than considered here. Gao et al. (2014) also examined the so-called “normalized helicity gradient variance” of Reinard et al. (2010) with results not substantially different from those obtained with the simpler helicity measurements.

The main result of our survey is that individual ARs, and averages made with superposed epoch analysis of ARs with respect to the times of strong flares, show mostly variations associated with (non-flare related) evolution. The similarity between the SPE results obtained for the two flux-density thresholds used also implies that most of these variations are restricted to the stronger flux regions near and within sunspots. Indeed, it appears challenging to remove this intrinsic variation in order to detect possible, specific, flare-related trends in the indices. The SPE analysis reduces much, but not all, evolution-related changes. Thus, even with nearly five years of high-quality data, it is apparently difficult to collect sufficient numbers of strong flares which also occur favorably close to the center of the disk to accommodate several days of helioseismic processing of both pre-flare and post-flare data. As we have noted, we performed additional SPE analysis with increased numbers of flares by reducing the time window around the flares. Our tests to date give essentially similar results. Namely, there are no temporal variations of the flow indices which are greater than observed in control tests with similar numbers of flares reassigned to random times.

Future work employing a wider parameter-search might be useful see whether flows with specific properties, or occurring within more restricted locations than the spatial masks used here, are more strongly correlated with flares. Such parameters could include properties of the flow field, the overlying magnetic field, and the vicinity (or connectivity of the field) to actual flare sites. A careful examination of individual case studies with data from HMI and other instruments could serve to guide this parameter selection.

We are grateful to Charles Baldner and the rest of Helioseismic and Magnetic Imager (HMI) team at Stanford University for computing and providing the custom datasets for this study. Many thanks to KD Leka for enlightening discussions and a careful read of a draft of the manuscript. We are also appreciative of the help-

ful suggestions made by the referee. This work is supported by the Solar Terrestrial program of the National Science Foundation through grant AGS-1127327 awarded to NWSA. Additional support is provided by the NASA Heliophysics program through contracts NNH12CF23C and NNH12CF68C. SDO data is provided courtesy of NASA/SDO and the AIA, EVE, and HMI science teams.

REFERENCES

- Baldner, C. S. & Schou, J. 2012, *ApJ*, 760, L1
 Beauregard, L., Verma, M., & Denker, C. 2012, *Astronomische Nachrichten*, 333, 125
 Birch, A. C., Braun, D. C., Leka, K. D., Barnes, G., & Javornik, B. 2013, *ApJ*, 762, 131
 Braun, D. C. 2014, *Sol. Phys.*, 289, 459
 Braun, D. C. & Birch, A. C. 2008, *ApJ*, 689, L161
 Braun, D. C., Birch, A. C., Benson, D., Stein, R. F., & Nordlund, A. 2007, *ApJ*, 669, 1395
 Braun, D. C., Birch, A. C., & Lindsey, C. 2004, in *SOHO 14 Helio- and Asteroseismology: Towards a Golden Future*, ed. D. Danesy, Vol. 559 (Noordwijk: ESA), 337–340
 Braun, D. C. & Wan, K. 2011, *J. Phys.: Conf. Ser.*, 271, 012007
 Brickhouse, N. S. & LaBonte, B. J. 1988, *Sol. Phys.*, 115, 43
 DeGrave, K., Jackiewicz, J., & Rempel, M. 2014, *ApJ*, 788, 127
 Duvall, Jr., T. L. & Gizon, L. 2000, *Sol. Phys.*, 192, 177
 Duvall, Jr., T. L. & Hanasoge, S. M. 2009, in *Solar-Stellar Dynamos as Revealed by Helio- and Asteroseismology: GONG 2008/SOHO 21*, ed. M. Dikpati, T. Arentoft, I. González Hernández, C. Lindsey, & F. Hill, Vol. 416 (San Francisco: Astron. Soc. Pacific), 103–109
 Fan, Y. 2009, *Liv Rev Solar Phys*, 1
 Gao, Y., Zhao, J., & Zhang, H. 2014, *Sol. Phys.*, 289, 493
 Gizon, L., Duvall, Jr., T. L., & Larsen, R. M. 2001, in *IAU Symposium, Vol. 203, Recent Insights into the Physics of the Sun and Heliosphere: Highlights from SOHO and Other Space Missions*, ed. P. Brekke, B. Fleck, & J. B. Gurman, 189–191
 Haber, D. A., Hindman, B. W., Toomre, J., Bogart, R. S., & Hill, F. 2001, in *SOHO 10/GONG 2000 Workshop: Helio- and Asteroseismology at the Dawn of the Millennium*, ed. A. Wilson & P. L. Pallé, Vol. 464 (ESA), 209–212
 Haber, D. A., Hindman, B. W., Toomre, J., & Thompson, M. J. 2004, *Sol. Phys.*, 220, 371
 Hindman, B. W., Haber, D. A., & Toomre, J. 2009, *ApJ*, 698, 1749
 Komm, R., Corbard, T., Durney, B. R., González Hernández, I., Hill, F., Howe, R., & Toner, C. 2004, *ApJ*, 605, 554
 Komm, R., Ferguson, R., Hill, F., Barnes, G., & Leka, K. D. 2011a, *Sol. Phys.*, 268, 389
 Komm, R. & Gosain, S. 2015, *ApJ*, 798, 20
 Komm, R. & Hill, F. 2009, *Journal of Geophysical Research (Space Physics)*, 114, 6105
 Komm, R., Howe, R., Hill, F., & Jain, K. 2011b, in *IAU Symposium, Vol. 273, The Physics of Sun and Star Spots*, ed. D. Prasad Choudhary & K. G. Strassmeier, 148–152
 Komm, R., Howe, R., Hill, F., Miesch, M., Haber, D., & Hindman, B. 2007, *ApJ*, 667, 571
 Leka, K. D. & Barnes, G. 2007, *ApJ*, 656, 1173
 Lindsey, C. & Braun, D. C. 1997, *ApJ*, 485, 895
 —. 2004, *ApJS*, 155, 209
 Mason, D., Komm, R., Hill, F., Howe, R., Haber, D., & Hindman, B. W. 2006, *ApJ*, 645, 1543
 Mason, J. P. & Hoeksema, J. T. 2010, *ApJ*, 723, 634
 Reinard, A. A., Henthorn, J., Komm, R., & Hill, F. 2010, *ApJ*, 710, L121
 Rüdiger, G., Brandenburg, A., & Pipin, V. V. 1999, *Astronom. Nach.*, 320, 135
 Schrijver, C. J. 2007, *ApJ*, 655, L117
 —. 2009, *Advances in Space Research*, 43, 739
 Wang, S., Liu, C., Deng, N., & Wang, H. 2014, *ApJ*, 782, L31
 Wang, S., Liu, C., & Wang, H. 2011, in *IAU Symposium, Vol. 273, The Physics of Sun and Star Spots*, ed. D. Prasad Choudhary & K. G. Strassmeier, 412–416
 Welsch, B. T., Li, Y., Schuck, P. W., & Fisher, G. H. 2009, *ApJ*, 705, 821

Zhao, J., Nagashima, K., Bogart, R. S., Kosovichev, A. G., &
Duvall, Jr., T. L. 2012, *ApJ*, 749, L5